

Piezomodulated-reflectivity study of minibands in $\text{Al}_x\text{Ga}_{1-x}\text{As}/\text{GaAs}$ superlattices

C. Parks and A. K. Ramdas

Department of Physics, Purdue University, West Lafayette, Indiana 47907

M. R. Melloch

School of Electrical Engineering, Purdue University, West Lafayette, Indiana 47907

L. R. Ram-Mohan*

*Departments of Physics, Electrical and Computer Engineering,
Worcester Polytechnic Institute, Worcester, Massachusetts 01609*

(Received 9 November 1992)

We report the observation of miniband formation in superlattices of $\text{Al}_x\text{Ga}_{1-x}\text{As}/\text{GaAs}$, grown by molecular beam epitaxy, manifested in their piezomodulated-reflectivity spectra when studied as a function of well (l_w) and barrier (l_b) widths. The piezomodulated-reflectivity spectra reveal signatures of well separated optical transitions both at the Brillouin zone center and at the zone boundary extending to energies above the $\text{Al}_x\text{Ga}_{1-x}\text{As}$ barrier. The clarity and sharpness of the spectral features allow an unambiguous identification of experimental transition energies with those calculated using the full eight-band $\mathbf{k}\cdot\mathbf{p}$ envelope-function approximation solved with the finite-element method. With $l_w = 25 \text{ \AA}$ [9 monolayers (ML)], $l_b = 20 \text{ \AA}$ (7 ML), and $x = 0.34$, the lowest energy transition at the miniband zone center and at the corresponding zone boundary are separated by 158 meV. With $l_w = 74 \text{ \AA}$ (26 ML) and $l_b = 45 \text{ \AA}$ (16 ML), the spectra correspond to quantum states in a multiple quantum well. Features associated with monolayer fluctuations in layer thickness are also observed.

I. INTRODUCTION

The quantum confined states of multiple quantum wells (MQW) of semiconductors evolve into superlattice minibands as the thickness of barriers separating the wells decreases, leading to an increasing coupling between quantum confined states. Miniband formation has been addressed theoretically¹ and experimentally demonstrated in photoluminescence excitation (PLE) spectra²⁻⁵ as well as in photomodulation spectra.⁶⁻⁸ The discovery and delineation of optical transitions characteristic of semiconductor heterostructures can be accomplished by exploiting a variety of modulation techniques. These include the piezomodulation⁹ or the photomodulation¹⁰ of the reflectivity spectra. While the photoluminescence spectrum provides valuable characterization, one observes only the lowest quantum confined transitions. The PLE spectroscopy does not suffer from this limitation and has indeed revealed an additional number of excited state transitions.¹¹ Quantum confined excitonic transitions within single, double, and multiple quantum wells⁹ as well as parabolic quantum wells;¹² quasibound features in asymmetric single quantum wells;^{13,14} and excitonic features in a pseudomorphic strained epilayer or strained layer heterostructures¹⁵⁻¹⁷ have been studied in III-IV and/or II-VI based heterostructures with piezomodulation and illustrate the versatility and power of the technique. The large spectral range covered, the freedom from photoexcited luminescence, the ease of measurements at any temperature

down to that of liquid helium, and, above all, the very high sensitivity in detecting signatures of optical transitions between a large number of quantum confined levels or minibands are the attractive features of the piezomodulation technique. It was felt that they could be advantageously exploited in the context of the superlattice electronic level structure. In particular, the desirability of extending previous studies beyond the first valence and conduction minibands in $\text{Al}_x\text{Ga}_{1-x}\text{As}$ superlattices provided a special motivation for the present investigation.

We have fabricated a series of such superlattices with dimensions selected for revealing the miniband formation as manifested in a piezomodulated-reflectivity spectrum. We have interpreted our results on the basis of a calculation of the electronic energy levels of the superlattices employing the full eight-band $\mathbf{k}\cdot\mathbf{p}$ Kane model Hamiltonian solved within the framework of the finite element method (FEM) and identified from the data involving transitions at the Brillouin zone center and edge of the minibands. Our goal is not to tailor the many input parameters of the $\mathbf{k}\cdot\mathbf{p}$ calculation to the individual characteristics of each sample in order to obtain precise agreement between theory and experiment. The goal is to justify the use of a generalized calculation with only three input parameters; the well and barrier layer thicknesses l_w and l_b , and the Al concentration.

II. THEORY

We consider planar layered semiconductor heterostructures with the planes perpendicular to the growth direc-

tion z . The layers are taken to be composed of compound III-V or II-VI semiconductors with their conduction- and valence-band edges located at the Γ point in the Brillouin zone (BZ). The periodic components of the Bloch functions, $u_{j,\mathbf{k}=0}(\mathbf{r})$ with j being the band index, at the band edges are assumed not to differ much as we traverse layer interfaces.¹ We assume that the original bulk crystal translational symmetry is maintained in the transverse direction.

We consider the zone-center bulk band structure of the constituent semiconductors, within the spirit of the $\mathbf{k} \cdot \mathbf{p}$ model. The usual eight-band model consists of the Γ_6 conduction band (c), the Γ_8 heavy-hole (hh) and light-hole (lh) bands, and the Γ_7 spin-orbit split-off band (s.o.), with their spin degeneracies. The in-plane dispersion in each layer is accounted for in our full calculations, as is the effect of strain arising from the small lattice mismatch between GaAs and $\text{Al}_x\text{Ga}_{1-x}\text{As}$. In the following brief outline of the theoretical procedure, we limit ourselves to the case with no external electric or magnetic fields or built-in strain in the layers. The following considerations

hold for the more general case with external perturbations except that the Kramers's degeneracy of the bands gets lifted, and the dimensions of the matrices are larger. The latter would be true also in the presence of strain. With this degeneracy and with the in-plane wave vector $(k_x, k_y) = 0$, the problem reduces to a three band model, with the hh band factoring out. The problem of solving for the envelope functions of the constituent layers, within the envelope function approximation (EFA), then reduces to the solution of a set of three simultaneous second order differential equations for the envelope functions. We have

$$H_{ij}(k_\perp, k_z) f_j(z) = E f_i(z), \quad (1)$$

where k_z has to be replaced by the differential operator $-i\frac{\partial}{\partial z}$, and $\mathbf{k}_\perp = (k_x, k_y)$ is the in-plane wave vector which is set to zero in the following.

The eigenvalues of the 3×3 matrix are given by the secular equation (in atomic units)

$$\begin{vmatrix} E_c + (F + \frac{1}{2})k_z^2 - E & -\sqrt{E_P/3}k_z & -\sqrt{E_P/6}k_z \\ -\sqrt{E_P/3}k_z & E_v - \frac{1}{2}(\gamma_1 + 2\gamma_2)k_z^2 - E & -\sqrt{2}\gamma_2 k_z^2 \\ -\sqrt{E_P/6}k_z & -\sqrt{2}\gamma_2 k_z^2 & E_s - \frac{1}{2}\gamma_1 k_z^2 - E \end{vmatrix} = 0. \quad (2)$$

Here E_c , E_v , and E_s are the band-edge energies of the conduction, lh, and the s.o. bands. The three coupled second order differential equations represented by Eq. (1) can be written as

$$\left(-\mathcal{A}_{ab} \frac{\partial^2}{\partial z^2} - i\mathcal{B}_{ab} \frac{\partial}{\partial z} + \mathcal{C}_{ab} \right) f_b(z) = E f_a(z). \quad (3)$$

The matrix coefficients $\mathcal{A}, \mathcal{B}, \mathcal{C}$ in Eq. (3) are assumed to be constant in each layer. In a heterostructure the differences in the band edge energies give rise to the confining potentials experienced by the carriers.

Equation (3) can be solved by the use of FEM for any arbitrary band edge profile. It has been shown by Ram-Mohan and co-workers that FEM can be adapted to yield *very accurate* eigenvalues for bound state problems,^{18,19} and for obtaining solutions of problems with complex geometries in quantum semiconductor heterostructures.^{20,21} In FEM, the heterostructure layers are split up into a number of "cells" or elements, in each of which the physical considerations of the problem hold. The eigenvalue problem, Eq. (1), is set up in each element by assuming that the wave functions are given locally in each element by fifth order Hermite interpolation polynomials, which have the property that the expansion coefficients correspond to the values of the wave function and its derivatives at select points, called nodes, in the element. The global wave functions $f_i(z)$ are constructed by joining the locally defined interpola-

tion functions and matching the function and its derivative across the element boundary for each of the bands included in the analysis. The *heterointerface* boundary conditions consisting of continuity of the functions and of the *probability current*, and the boundary conditions for the bound states at $z = \pm\infty$ are readily incorporated into the FEM. The element matrices are overlaid into a global matrix in a manner consistent with the boundary conditions. The resultant global eigenvalue problem is a generalized eigenvalue problem which is solved for the eigenenergies and wave functions with a standard diagonalizer on a workstation. Additional details are planned to be presented elsewhere.²²

The use of three elements per layer leads to very accurate quantum well energies and eigenfunctions in the FEM. The eigenvalues of the FEM agree with those obtained from the eight-band transfer matrix method²³⁻²⁶ to within 10^{-6} eV; the results can be obtained with double precision accuracy by employing more elements in the computation. As mentioned earlier, the results reported here are from calculations which include effects of strain from the small lattice mismatch between GaAs and $\text{Al}_{1-x}\text{Ga}_x\text{As}$.

The results of the FEM computation on an $\text{Al}_{0.31}\text{Ga}_{0.69}\text{As}/\text{GaAs}$ superlattice are shown in Fig. 1 where the barrier layer thickness (l_b) is 10 monolayers (1 ML = 2.83 Å) and the well layer thickness (l_w) is 18 ML. The left panel shows the dispersion along the growth direction and the right panel is the dispersion perpendic-

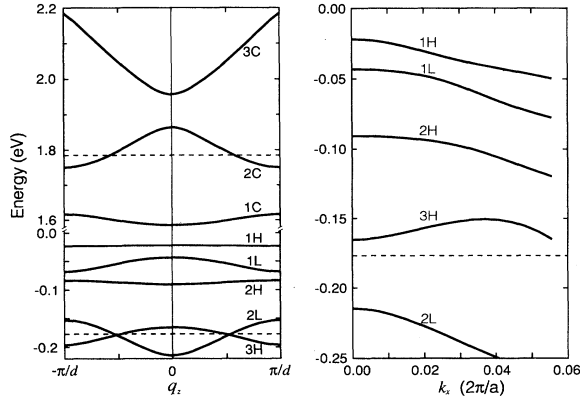


FIG. 1. The superlattice conduction bands and valence bands in the first Brillouin zone as computed by the FEM for sample no. 1. The energies are measured relative to the bulk GaAs valence-band edge. The dashed lines indicate the energy of the $\text{Al}_{0.31}\text{Ga}_{0.69}\text{As}$ conduction- and valence-band edges. The left panel is the superlattice dispersion along the growth direction and the right panel is the dispersion perpendicular to the growth direction.

ular to the growth direction. The dispersion for the conduction band along the k_x direction is not shown as it is parabolic for all minibands near $k_x = 0$. The thin barriers result in strong coupling between neighboring GaAs wells to form superlattice minibands along the k_z direction. Strong direct ($q_z^{\text{initial}} = q_z^{\text{final}}$) optical transitions in piezomodulated spectra originate from a critical point in the valence band to that in the conduction band. Such critical points occur at both the center $q_z = 0$ and edge $q_z = 1$ (in units of π/d where $d = l_w + l_b$) of the superlattice Brillouin zone. There exist two types of three-dimensional critical points for each miniband in Fig. 1. These include M_0 -type critical points (extrema) as well as M_1 -type critical points (saddle points). Most transitions in the piezomodulated spectra are direct transitions between two M_0 or two M_1 critical points. The one exception is the third hh miniband, i.e., the $3H$ miniband where the direct transition at $q_z = k_x = 0$ is from an M_1 to an M_0 critical point. While there is another $3H$ miniband critical point away from $k_x = 0$, transitions from this critical point would be indirect and should be weaker than the direct transition in the piezomodulated spectra.

III. EXPERIMENT

The superlattices used in this work were grown in a Varian GEN II molecular beam epitaxy (MBE) system on two-in. diam., undoped, liquid-encapsulated-Czochralski (100)-GaAs substrates obtained from Airtron.²⁷ The substrates were degreased, etched in a 60 °C solution of 5:1:1 of $\text{H}_2\text{SO}_4:\text{H}_2\text{O}_2:\text{H}_2\text{O}$ for 1 min, and placed in a nonbonded substrate mount. The substrates were outgassed for 2 h at 200 °C in the entry chamber of the MBE apparatus and then moved to the buffer chamber. Each substrate was outgassed for 1 h at 300 °C in the buffer chamber immediately before being loaded into the growth chamber. In the growth chamber, each sample was heated to 615 °C for 2 min (the surface oxides desorbed at 580 °C) and then the substrate temperature was lowered to the initial growth temperature of 600 °C. A 0.5 μm GaAs buffer layer was grown at a rate of 1 $\mu\text{m}/\text{h}$ and an As_2 to Ga beam equivalent pressure of 18. While continuing to grow GaAs, the Ga flux was then decreased to a growth rate of 0.7 $\mu\text{m}/\text{h}$ and the substrate temperature lowered to 590 °C. This was followed by a 50 period superlattice consisting of GaAs wells and $\text{Al}_x\text{Ga}_{1-x}\text{As}$ barriers. The superlattices were grown without any interruptions between layers which are sometimes used to provide for smooth heterojunction interfaces.²⁸ The layer thicknesses for each superlattice are given in Table I. The nominal layer thicknesses and Al concentrations were obtained from the MBE growth calibration. The layer thicknesses are specified in units of one monolayer.

The piezomodulated-reflectivity spectrum of the superlattices was achieved by fixing the GaAs substrate to a 2 mm thick lead-zirconate-titanate (PZT) transducer driven by a 560 V sinusoidal voltage. The alternating expansion and contraction of the transducer induced a rms strain of $\sim 10^{-5}$. A Janis SuperTran²⁹ optical cryostat was employed with liquid helium as a coolant. The light from a 600 W tungsten halogen lamp was passed through a Perkin-Elmer (model E-1) double-pass grating monochromator. A 4950 Å long-pass filter was used to eliminate the diffracted light in the second order from the region of interest. A uv-enhanced Si photodiode detected the reflected light. The modulated component (ΔR) of the reflected spectrum was isolated by a lock-in amplifier. The operation of the monochromator and collection of the data were carried out with a microcomputer.³⁰

TABLE I. The thicknesses of the well (l_w) and barrier (l_b) layers of the superlattices were obtained from a fit of the FEM calculation to experiment. The Al concentration (x) of the barrier layers is directly from experiment. The energies of the $11H^0$ luminescence peak and its FWHM are also given. The nominal sample parameters from the MBE growth calibration are in brackets.

Sample no.	l_w (ML)	l_b (ML)	x	$11H^0$ (eV)	FWHM (meV)
1	18 [18]	10 [9]	0.31 [0.30]	1.6040	1.6
2	27 [27]	10 [9]	0.28 [0.30]	1.5658	1.5
3	9 [9]	7 [7]	0.34 [0.30]	1.6680	2.5
4	26 [27]	16 [18]	0.33 [0.30]	1.5751	1.7

IV. RESULTS AND DISCUSSION

The photoluminescence spectrum of each superlattice was recorded in order to provide a characterization of the sample parameters and quality of the fabrication. Figure 2 shows the photoluminescence spectra for the four superlattices recorded at a temperature of 8 K with an excitation wavelength of 5145 Å and power of 40 mW/cm². Table I lists the energies and full width at half maximum (FWHM) of the photoluminescence peaks of each superlattice. The photoluminescence peaks are from the free exciton recombination associated with transitions from the first superlattice conduction band to the first heavy-hole valence band (11H⁰ transition). Since the Al concentrations (x) of the barriers are approximately equal, the differences in the position of the photoluminescence peaks in Fig. 2 are a result of the differing well and barrier thickness. The sharpness of the photoluminescence peaks indicates the superlattices are of the highest quality.

Figure 3 shows the piezomodulated-reflectivity spectrum of superlattice no. 1. The feature labeled A⁰ at 1.494 eV is attributed to a residual acceptor associated with neutral carbon having a binding energy of 25 meV.³¹ The signature of the GaAs buffer layer is located at 1.5160±0.0003 eV. These two features are present in the spectra of all the four superlattices. The remaining features in the spectrum arise from superlattice interband transitions.

The transitions are labeled as $nm(H, L)$ where n and m identify the superlattice conduction band and the superlattice valence band, respectively, with H and L denoting the heavy-hole or light-hole band. The superscript 0 or 1 indicates a transition at $q_z = 0$ or at $q_z = 1$, respectively. The transitions at $q_z = 0$ between odd numbered bands

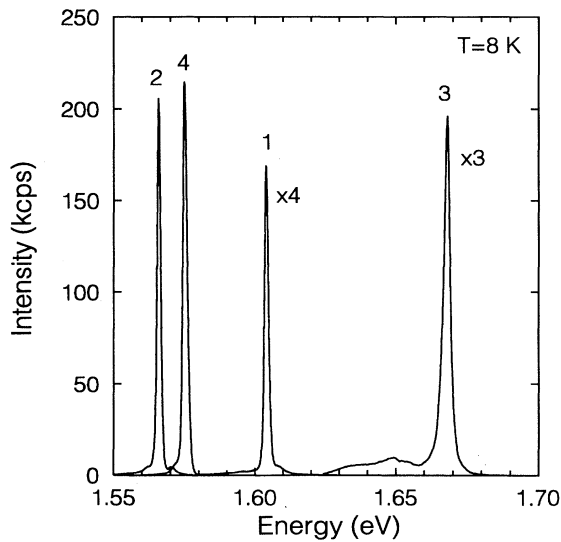


FIG. 2. Photoluminescence spectra of the 11H⁰ transition for the superlattices tabulated in Table I. The spectra were recorded at a temperature of $T = 8$ K and excited with the 5145 Å line of an Ar⁺ laser.

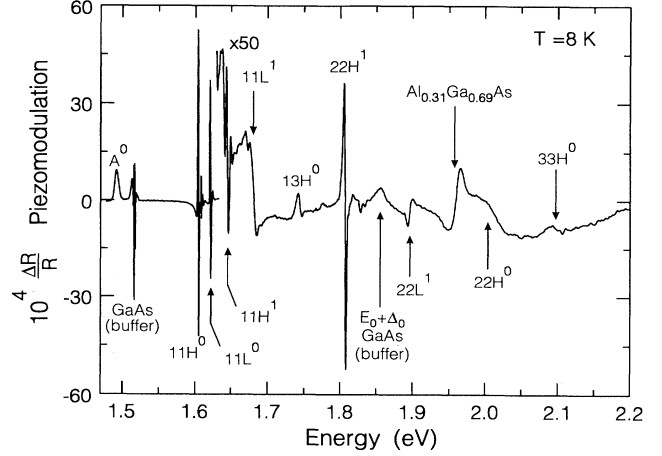


FIG. 3. The piezomodulated-reflectivity spectrum of the Al_{0.31}Ga_{0.69}As/GaAs superlattice sample no. 1 with a 28.3 Å (10 ML) barrier and 50.9 Å (18 ML) well. The spectrum was recorded at $T = 8$ K.

and those at $q_z = 1$ between even numbered bands correspond to transitions between M_0 critical points. On the other hand, the transitions at $q_z = 0$ between even numbered bands and those at $q_z = 1$ between odd numbered bands are transitions between M_1 critical points. One exception is the transitions involving the 3H miniband at $q_z = 0$ as mentioned earlier. Thus 11H⁰, 11L⁰, 22H¹, and 22L¹ are M_0 transitions and 11H¹, 11L¹, 22H⁰, and 22L⁰ are M_1 transitions. The 13H⁰ and 33H⁰ transitions are between an M_0 and M_1 critical point.

The energy of each intersubband transition is given by

$$E_{n,m} = E_g + E_n + E_m - E_{n,m}^B, \quad (4)$$

where E_g is the band gap of GaAs, E_n is the energy of the n th conduction band, E_m is the energy of the m th heavy-hole or light-hole valence band, and $E_{n,m}^B$ is the binding energy of the exciton in the superlattice with its two-dimensional characteristics.

The experimental transition energies were obtained from a fit of the data to the first derivative Lorentzian line shape for excitons. The normalized piezomodulated reflectivity can be expressed by³²

$$\frac{\Delta R}{R} = \alpha \Delta \epsilon_r + \beta \Delta \epsilon_i, \quad (5)$$

where α and β are the Seraphin coefficients, and $\Delta \epsilon_r$ and $\Delta \epsilon_i$, respectively, are the change of the real and imaginary parts of the dielectric constants as a result of the change in the energy gap of the sample due to a stress. For a spectrum in the vicinity of an n -dimensional critical point the change of the complex dielectric constant resulting from the stress modulation is given by³³

$$\frac{d\epsilon(E)}{dE_g} = -i^{r-n} C_n (E - E_g + i\Gamma)^{(n/2)-2}, \quad (6)$$

where C_n is the spectral amplitude which is proportional

to the square of the momentum matrix, E is the photon energy, E_g is the energy of the transition, Γ is the Lorentzian broadening parameter, and r corresponds to the M_r critical point. For discrete excitons n is zero. In order to maintain consistency in setting the transition energy uncertainties, we define the uncertainty as $\Gamma/2$.

Consistent with the $11H^0$ transition energy in the photoluminescence spectrum, the two intense features in Fig. 3 at 1.6045 eV and 1.6207 eV may be unambiguously assigned to the $11H^0$ and $11L^0$ transitions. Furthermore, the energy and the intensity of the strong and sharp feature at 1.8067 eV indicates that it arises from the $22H^1$ transition. With these constraints, we now adjust only two input parameters in the FEM calculation, the well and barrier thickness, in order to obtain agreement between theory and experiment. We also restrict the layer thicknesses to be integral multiples of one monolayer. The Al content of the barrier layer is fixed by the feature at 1.959 eV which is attributed to the $\text{Al}_{0.31}\text{Ga}_{0.69}\text{As}$ barrier (cap) layer. The calibration of Al content was achieved by utilizing the expression of Bosio *et al.*³⁴ for the excitonic energy gap of $\text{Al}_x\text{Ga}_{1-x}\text{As}$. All other material parameters for the calculations were obtained from the standard sources³⁵ and were not adjusted to provide better agreement between theory and experiment. A conduction-band offset of 60% was used for all calculations.

The feature at 1.862 eV in Fig. 3 is attributed to a transition between the Γ_7 spin-orbit split-off band to the Γ_6 conduction band in the GaAs buffer layer. A comparison between the experimental and theoretical transition energies is presented in Table II. The exciton binding energy which would lower the theoretical transition energies has not been included in the theoretical calculations.

As mentioned earlier, each miniband is characterized by an M_0 and M_1 critical point. Figure 3 clearly exhibits interband transitions which can be identified as those between the M_1 saddle points of two conduction and three valence minibands: $1H^1$, $1L^1$, $1C^1$, $2H^0$, and $2C^0$. The thin barriers and narrow wells of this superlattice result in the formation of wide minibands. Consequently, the $11H^1$ and $11L^1$ M_1 transitions are well separated from the more intense $11H^0$ and $11L^0$ M_0 transitions between the same minibands. The magnitude of the separation

TABLE II. The experimental and theoretical transition energies (eV) of superlattice no. 1. The theoretical values have not been corrected for exciton binding energies.

Experimental	Theory	Identification
1.6045 ± 0.0004	1.607	$11H^0$
1.6207 ± 0.0004	1.628	$11L^0$
1.6439 ± 0.0020	1.640	$11H^1$
1.6805 ± 0.0046	1.684	$11L^1$
1.7407 ± 0.0026	1.750	$13H^0$
1.8067 ± 0.0011	1.834	$22H^1$
1.8950 ± 0.0025	1.903	$22L^1$
1.959 ± 0.006		$\text{Al}_{0.31}\text{Ga}_{0.69}\text{As}$
2.013 ± 0.015	1.954	$22H^0$
2.090 ± 0.005	2.122	$33H^0$

allows unambiguous assignments which exclude the possibility of confusion with monolayer fluctuations or $2s$ excitons.^{36,28,37} We shall discuss this point later in this section. We also observe a transition labeled $22H^0$ which is above the $\text{Al}_{0.31}\text{Ga}_{0.69}\text{As}$ barrier energy. We may determine if the M_1 transitions are excitonic by considering the line shape of the transition.^{38,39} The $11H^1$ transition line shape is excitonic while the $11L^1$ and $22H^0$ are, in contrast, more interbandlike.

Figure 4 shows the probability density of the wave function for each energy level at the BZ center, $q_z = 0$ and at the BZ edge, $q_z = \pi/d$. The first energy levels do not show a significant degree of barrier penetration despite the narrow 28 Å (10 ML) barrier. On the other hand, the second conduction miniband $2C^1$ at the BZ edge just below the barrier energy shows strong barrier penetration. It is this level which results in the sharp $22H^1$ transition in Fig. 3. The third conduction miniband $3C^0$ at the BZ center shows a high probability density in the barrier layer and not the GaAs well layer. There is still a considerable overlap between the third heavy-hole and third conduction minibands because the $3H^0$ level shows a large degree of barrier penetration. Localization within the barrier layer of some above barrier states has been confirmed by measurements of Zeeman splitting in heterostructures composed of diluted magnetic semiconductors.⁴⁰

We now turn to the the piezomodulated-reflectivity spectrum of superlattice no. 2 shown in Fig. 5. Comparison of Figs. 3 and 5 shows the effect of reducing the well thickness while keeping the barrier thickness constant. As expected, all transitions observed in superlattice no. 1 appear at lower energies. We once again observe the $11L^1$ M_1 transition. The calculated positions of the $11H^1$ and $22H^0$ transitions lie very close to the $11L^0$ and $22L^1$ transitions and hence preclude their observation. In contrast to the $11L^1$ line in Fig. 3, the $11L^1$

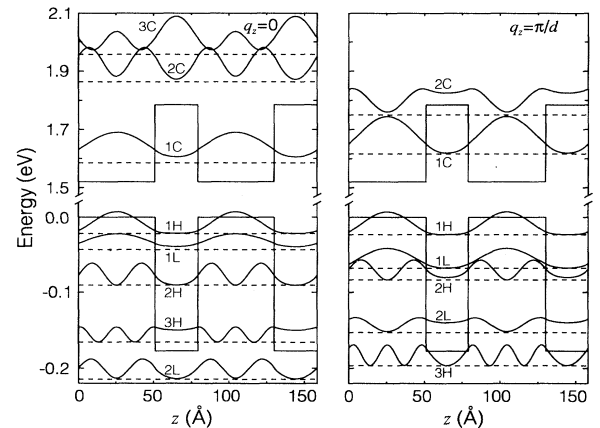


FIG. 4. A plot of the probability density (curves) of each critical point energy (dashed lines) for superlattice sample no. 1. The probability density is shown for the BZ center ($q_z = 0$) and the BZ edge ($q_z = \pi/d$). The square potential profile of the superlattice is also shown. The energies are measured relative to the bulk GaAs valence-band edge.

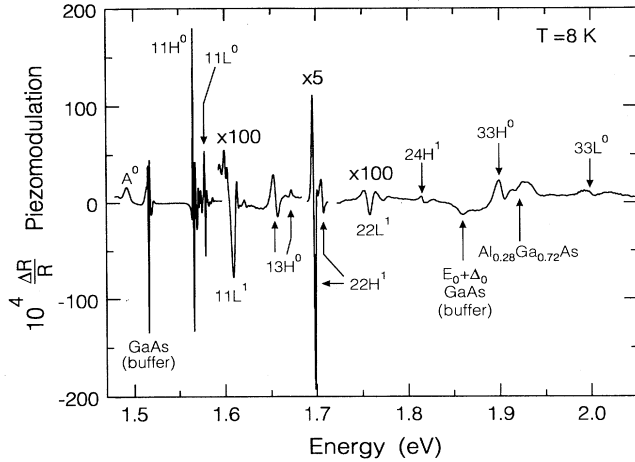


FIG. 5. The piezomodulated-reflectivity spectrum of the $\text{Al}_{0.28}\text{Ga}_{0.72}\text{As}/\text{GaAs}$ superlattice sample no. 2 with a 28.3 Å (10 ML) barrier and 76.3 Å (27 ML) well. The spectrum was recorded at $T = 8$ K.

transition here has a line shape normally associated with an excitonic transition. The $33H^0$ transition has moved below the $\text{Al}_{0.28}\text{Ga}_{0.72}\text{As}$ barrier energy while the $33L^0$ transition is now sufficiently intense to be observed above the barrier energy. Table III lists the experimental and theoretical values for the transition energies. The agreement between theory and experiment for this superlattice is excellent over the entire energy range from 1.5 eV to 2.0 eV, including the $33L^0$ transition above the barrier.

A more dramatic example of superlattice miniband dispersion is presented in Fig. 6 where $l_w = 25$ Å (9 ML) and $l_b = 20$ Å (7 ML) giving a total period of just $d = 45$ Å. The narrow wells and barriers result in a large barrier penetration. With these parameters there is only one conduction miniband, $1C$, with a very large energy spread of 146 meV. The $11H^1$ and $11L^1$ M_1 critical points are easily identified in Fig. 6 on the basis of the theoretical and experimental transition energies listed in Table IV. The $22H^1$ transition is now to a conduction band state above the barrier and has lost the sharpness and clarity of such a transition in the other superlattices. Al-

TABLE III. The experimental and theoretical transition energies (eV) of superlattice no. 2. The theoretical values have not been corrected for exciton binding energies.

Experimental	Theory	Identification
1.5657 ± 0.0005	1.569	$11H^0$
1.5783 ± 0.0005	1.584	$11L^0$
1.6084 ± 0.0032	1.613	$11L^1$
1.6548 ± 0.0023	1.654	$13H^0$
1.6968 ± 0.0011	1.708	$22H^1$
1.7576 ± 0.0015	1.759	$22L^1$
1.8151 ± 0.0018	1.819	$24H^1$
1.9016 ± 0.0042	1.906	$33H^0$
1.910 ± 0.011		$\text{Al}_{0.28}\text{Ga}_{0.72}\text{As}$
1.9978 ± 0.0065	1.991	$33L^0$

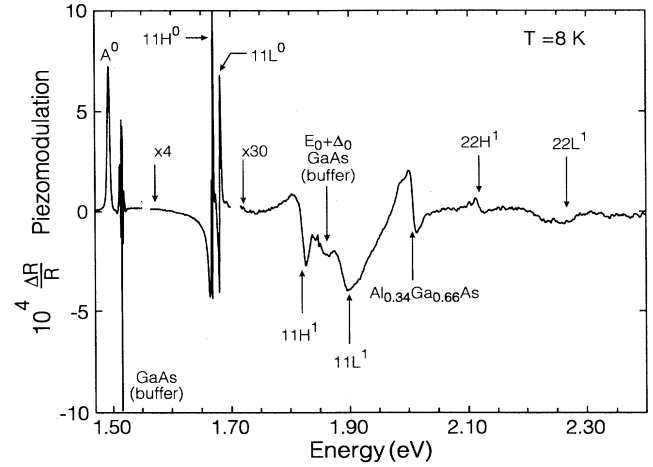


FIG. 6. The piezomodulated-reflectivity spectrum of the $\text{Al}_{0.34}\text{Ga}_{0.66}\text{As}/\text{GaAs}$ superlattice sample no. 3 with a 19.8 Å (7 ML) barrier and 25.4 Å (9 ML) well. The spectrum was recorded at $T = 8$ K.

though the $11H^0$ photoluminescence peak is still sharp (see Fig. 2), it is somewhat broader than those in the other superlattices; this may be caused by unavoidable difficulties in the fabrication of superlattices with such thin layers.

In progressing from superlattice no. 2 to superlattice no. 4 we have maintained the same well thickness of ~ 75 Å (26 ML) while the barrier thickness is increased to 45 Å (16 ML). Figure 7 shows the piezomodulated-reflectivity spectrum of superlattice no. 4. A comparison of Figs. 5 and 7 shows that by increasing the barrier thickness, the transition energies are shifted to slightly higher energies. Table V lists the theoretical and experimental transition energies in superlattice no. 4. The spectrum of each

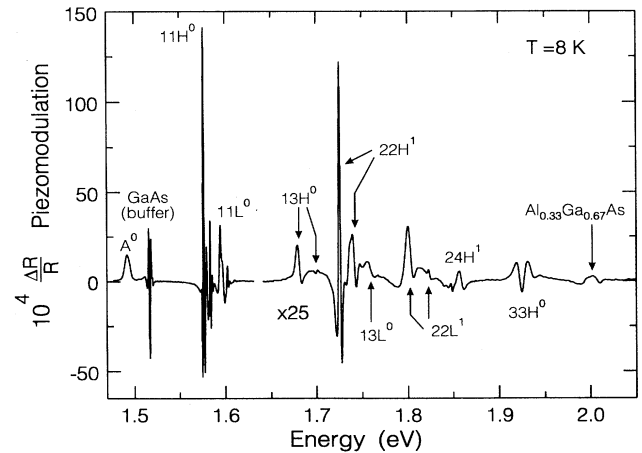


FIG. 7. The piezomodulated-reflectivity spectrum of the $\text{Al}_{0.33}\text{Ga}_{0.67}\text{As}/\text{GaAs}$ superlattice sample no. 4 with a 45.2 Å (16 ML) barrier and 73.5 Å (26 ML) well. Multiple features given the same label are due to monolayer fluctuations in layer thickness. The spectrum was recorded at $T = 8$ K.

TABLE IV. The experimental and theoretical transition energies (eV) of superlattice no. 3. The theoretical values have not been corrected for exciton binding energies.

Experimental	Theory	Identification
1.6687±0.0008	1.685	11H ⁰
1.6804±0.0009	1.704	11L ⁰
1.827±0.005	1.844	11H ¹
1.900±0.010	1.947	11L ¹
2.000±0.011		Al _{0.34} Ga _{0.66} As
2.115±0.007	2.128	22H ¹
2.282±0.008	2.233	22L ¹

superlattice reveals that the dominant transitions occur between minibands where the band index n changes by $\Delta n = 0, 2$ with $\Delta q_z = 0$.

Piezomodulated reflectivity is also capable of revealing the uniformity of the superlattice layer thicknesses. This is demonstrated by examining Fig. 8 which is an expanded view of the 11H⁰ and 11L⁰ transitions of Fig. 7. Each transition consists of one large feature closely followed by smaller features at a slightly higher energy. We attribute these additional features to monolayer fluctuations in the layer thicknesses of the superlattice. We exclude a 2s exciton as an interpretation because it should be much weaker than the features in Fig. 8 and, in addition, would not account for all of the features. See Ref. 14 for the relative intensity of the 2s to 1s excitonic features in a piezomodulated-reflectivity spectrum. These additional features associated with monolayer fluctuations are usually present in the spectra of single quantum wells fabricated with growth interruptions.²⁸ In the case of the superlattices, the fluctuations can be from one layer thickness to the next across all the 50 periods as well as from monolayer fluctuations at each interface. In single quantum wells the latter case will influence the

TABLE V. The experimental and theoretical transition energies (eV) of superlattice no. 4. The GaAs layer thickness from which each transition in Figs. 7 and 8 originates is given in monolayers (ML). The theoretical values have not been corrected for exciton binding energies.

Experimental	Theory	Identification	Thickness
1.5753±0.0004	1.581	11H ⁰	26
1.5787±0.0009	1.585	11H ⁰	25
1.5829±0.0004	1.589	11H ⁰	24
1.5947±0.0006	1.602	11L ⁰	26
1.5975±0.0012	1.607	11L ⁰	25
1.6024±0.0006	1.612	11L ⁰	24
1.6795±0.0020	1.678	13H ⁰	26
1.7000±0.0020	1.698	13H ⁰	24
1.7249±0.0012	1.743	22H ¹	26
1.7428±0.0015	1.768	22H ¹	24
1.7562±0.0027	1.773	13L ⁰	26
1.8004±0.0054	1.808	22L ¹	26
1.8556±0.0020	1.871	24H ¹	26
1.9233±0.0029	1.943	33H ⁰	26
1.993±0.005		Al _{0.33} Ga _{0.67} As	
2.0090±0.0025	2.038	33L ⁰	26

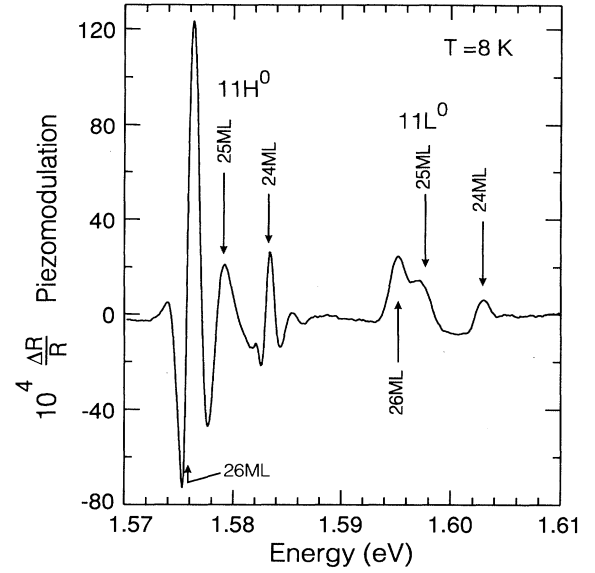


FIG. 8. An enlarged view of the 11H⁰ and 11L⁰ transitions of sample no. 4. Additional features are attributed to GaAs layer thickness of 26 to 24 monolayers and are labeled with their experimental transition energies. The total superlattice period is $d = 118.7 \text{ \AA}$ (42 ML).

spectra whereas the former is most likely to manifest in superlattices, i.e., in superlattices, the effects associated with monolayer fluctuations at a given interface may be expected to be averaged over the entire superlattice. For the sample in Fig. 8 the intensity of the features indicates most layers are 26 ML thick with the remainder being 25 and 24 ML thick. The features associated with monolayer fluctuations also appear for higher transition energies such as 13H⁰ and 22H¹. Superlattices no. 2 (Fig. 5) and no. 4 (Fig. 7) clearly exhibit features associated with monolayer fluctuations. Superlattice no. 1 (Fig. 3) shows a remarkable degree of uniformity with clean 11H⁰ and 11L⁰ features having just one small additional feature corresponding to a one monolayer fluctuation. The features associated with monolayer fluctuations must be carefully considered when attempting to determine the existence of M_1 critical points, otherwise features may be mistakenly identified. The 11H¹ M_1 transition is expected 4 meV above the 11H⁰ M_0 transition and may be present in Fig. 8 but they cannot be confidently separated from the stronger features arising from monolayer fluctuations. Indeed, the band formation in this superlattice appears to be that of a multiple quantum well.

V. CONCLUDING REMARKS

The miniband formation and M_1 critical point transitions in superlattices have been observed unambiguously in the piezomodulated-reflectivity spectra. The comparison between theory and experiment gives confirmation

of the identification of the spectral features corresponding to the BZ center and BZ boundary. Furthermore, piezomodulated reflectivity has been shown to be a useful tool for characterizing the uniformity of the layer thicknesses.

We draw attention to the work reported by Peterson *et al.*,⁷ where the authors have observed in the room temperature photomodulated spectrum the miniband formation in a superlattice of $\text{Al}_{0.28}\text{Ga}_{0.72}\text{As}/\text{GaAs}$ with wide wells ($> 250 \text{ \AA}$) and narrow barriers ($\sim 17 \text{ \AA}$). The large well width resulted in many closely spaced transitions with noticeable widths for the minibands occurring only for higher-energy states, which makes theoretical comparisons more challenging. The parameters used in the present work permitted a study of the miniband formation as a function of well and barrier width. The sensitivity of the piezomodulation technique and the measurements at $T = 8 \text{ K}$ have resulted in sharp signatures whose energies can be compared with those predicted by the eight-band $\mathbf{k}\cdot\mathbf{p}$ envelope-function approximation implemented by the FEM. Note that even the $11H^0$ and $11H^1$ signatures of the superlattice with $l_w = 25 \text{ \AA}$ (9 ML) and $l_b = 20 \text{ \AA}$ (7 ML) are separated by as much as 158 meV, and the $11L^0$ and $11L^1$ signatures are separated by 220 meV. The miniband formation is brought out in a particularly striking fashion in the superlattices with thin layers and the corresponding small number of

confined states as illustrated in Figs. 3 and 6.

We have demonstrated that the envelope function approximation solved within the framework of the FEM provides a reliable prediction of superlattice miniband energies over a large energy range, including above barrier minibands which may be exploited in the implementation of photodetectors.⁴¹ It is possible to achieve a better correlation between theory and experiment by slightly adjusting the many input parameters to the calculation. However, we limited ourselves to adjusting *only* the well and barrier layer thicknesses in order to provide a meaningful comparison between theory and experiment and to show more convincingly the ability of the theory to predict transition energies before fabricating a superlattice.

ACKNOWLEDGMENTS

We wish to thank Quantum Semiconductor Algorithms (QSA) for the use of their software for energy level calculations. The investigation at WPI has been supported by the Strategic Defense Initiative of the Innovative Science and Technology Office (SDI-ISTO) administered by the U.S. Naval Research Laboratory under Grant No. N00014-87-K-2031-LRR and the work at Purdue has been supported by the National Science Foundation, Grant No. DMR-89-21717 (C.P. and A.K.R.).

* Also at Naval Research Laboratory, 4555 Overlook Avenue, Washington, D.C. 20375-5000.

¹ See, for example, G. Bastard, *Wave Mechanics Applied to Semiconductor Heterostructures* (Les Editions de Physique, Les Ulis, France, 1988).

² J. J. Song, Y. S. Yoon, A. Fedotowsky, Y. B. Kim, J. N. Schulman, C. W. Tu, D. Huang, and H. Morkoc, *Phys. Rev. B* **34**, 8958 (1986).

³ J. J. Song, P. S. Jung, Y. S. Yoon, Hanyou Chu, Yia-Chung Chang, and C. W. Tu, *Phys. Rev. B* **39**, 5562 (1989).

⁴ B. Deveaud, A. Chomette, F. Clérot, A. Regreny, J. C. Maan, R. Romestain, G. Bastard, Hanyou Chu, and Yia-Chung Chang, *Phys. Rev. B* **40**, 5802 (1989).

⁵ K. J. Moore, G. Duggan, K. Woodbridge, C. Roberts, N. J. Pulsford, and R. J. Nicholas, *Phys. Rev. B* **42**, 3024 (1990).

⁶ H. Shen, S. H. Pan, F. H. Pollak, M. Dutta, and T. R. AuCoin, *Phys. Rev. B* **36**, 9384 (1987).

⁷ M. W. Peterson, J. A. Turner, C. A. Parsons, A. J. Nozik, D. J. Arent, C. Van Hoof, G. Borghs, R. Houdré, and H. Morkoc, *Appl. Phys. Lett.* **53**, 2666 (1988).

⁸ C. Vazquez-Lopez, E. Ribeiro, F. Cerdeira, P. Motisuke, M. A. Scilotti, and A. P. Roth, *J. Appl. Phys.* **69**, 7836 (1991).

⁹ Y. R. Lee, A. K. Ramdas, F. A. Chambers, J. M. Meese, and L. R. Ram-Mohan, *Appl. Phys. Lett.* **50**, 600 (1987).

¹⁰ O. J. Glembocki and B. V. Shanabrook, in *Semiconductors and Semimetals*, edited by R. K. Willardson, A. C. Beer, and E. R. Weber (Academic, San Diego, 1992), Vol. 36, p. 222.

¹¹ See, for example, R. C. Miller, A. C. Gossard, D. A. Kleinman, and O. Munteanu, *Phys. Rev. B* **29**, 3740 (1984).

¹² Y. R. Lee, A. K. Ramdas, A. L. Moretti, F. A. Chambers,

G. P. Devane, and L. R. Ram-Mohan, *Phys. Rev. B* **41**, 8380 (1990).

¹³ D. Dossa, Lok C. Lew Yan Voon, L. R. Ram-Mohan, C. Parks, R. G. Alonso, A. K. Ramdas, and M. R. Melloch, *Appl. Phys. Lett.* **59**, 2706 (1991).

¹⁴ C. Parks, R. G. Alonso, A. K. Ramdas, L. R. Ram-Mohan, D. Dossa, and M. R. Melloch, *Phys. Rev. B* **45**, 14215 (1992).

¹⁵ Y. R. Lee, A. K. Ramdas, L. A. Kolodziejski, and R. L. Gunshor, *Phys. Rev. B* **38**, 13143 (1988).

¹⁶ R. L. Harper, Jr., R. N. Bicknell, D. K. Blanks, N. C. Giles, J. F. Schetzina, Y. R. Lee, and A. K. Ramdas, *J. Appl. Phys.* **65**, 624 (1988).

¹⁷ R. G. Alonso, C. Parks, A. K. Ramdas, H. Luo, N. Samarth, J. K. Furdyna, and L. R. Ram-Mohan, *Phys. Rev. B* **45**, 1181 (1992).

¹⁸ L. R. Ram-Mohan, S. Saigal, D. Dossa, and J. Shertzer, *Comput. Phys.* **4**, 50 (1990), and references therein.

¹⁹ J. Shertzer, L. R. Ram-Mohan, and D. Dossa, *Phys. Rev. A* **40**, 4777 (1989).

²⁰ J. Shertzer and L. R. Ram-Mohan, *Phys. Rev. B* **41**, 9994 (1990).

²¹ L. R. Ram-Mohan and J. Shertzer, *Appl. Phys. Lett.* **57**, 282 (1990).

²² L. R. Ram-Mohan (unpublished).

²³ L. R. Ram-Mohan, K. H. Yoo, and R. L. Aggarwal, *Phys. Rev. B* **38**, 6151 (1988).

²⁴ K. H. Yoo, R. L. Aggarwal, and L. R. Ram-Mohan, *J. Vac. Sci. Technol. A* **7**, 415 (1989).

²⁵ K. H. Yoo, L. R. Ram-Mohan, and D. F. Nelson, *Phys. Rev. B* **39**, 12808 (1989).

²⁶ B. Chen, M. Lazzouni, and L. R. Ram-Mohan, *Phys. Rev.*

- B **45**, 1204 (1992).
- ²⁷ Airtron, 200 East Hanover Ave., Morris Plains, NJ 07950.
- ²⁸ M. A. Herman, D. Bimberg, and J. Christen, *J. Appl. Phys.* **70**, R1 (1991).
- ²⁹ Janis "Super Varitemp" Model 10DT, Janis Research, Inc., P.O. Box 696, 2 Jewel Ave., Wilmington, MA 01887-0896.
- ³⁰ For further details see Y. R. Lee, Ph.D. thesis, Purdue University, 1987.
- ³¹ C. E. C. Wood, in *Molecular Beam Epitaxy and Heterostructures*, edited by L. L. Chang and K. Ploog (Nijhoff, Dordrecht, 1985), p. 149; A. Y. Cho, in *ibid.*, p. 191.
- ³² B. O. Seraphin and N. Bottka, *Phys. Rev.* **145**, 628 (1966).
- ³³ M. Okuyama, T. Nishino, and Y. Hamakawa, *J. Phys. Soc. Jpn.* **35**, 134 (1973).
- ³⁴ C. Bosio, J. L. Staehli, M. Guzzi, G. Burri, and R. A. Logan, *Phys. Rev. B* **38**, 3263 (1988).
- ³⁵ *Landolt-Börnstein Numerical Data and Functional Relationships in Science and Technology*, edited by O. Madelung, M. Schulz, and H. Weiss, Landolt-Börnstein, New Series, Group III, Vol. 17a (Springer, Berlin, 1982).
- ³⁶ B. Deveaud, J. Y. Emery, A. Chomette, B. Lambert, and M. Baudet, *Appl. Phys. Lett.* **45**, 1078 (1984).
- ³⁷ D. F. Nelson, R. C. Miller, C. W. Tu, and S. K. Spitz, *Phys. Rev. B* **36**, 8063 (1987).
- ³⁸ E. Matatagui, A. G. Thompson, and M. Cardona, *Phys. Rev.* **176**, 950 (1968).
- ³⁹ M. Cardona, *Modulation Spectroscopy*, Suppl. 11 of *Solid State Physics*, edited by F. Seitz, D. Turnbull, and H. Ehrenreich (Academic, New York, 1969), p. 137.
- ⁴⁰ F. C. Zhang, N. Dai, H. Luo, N. Samarth, M. Dobrowolska, J. K. Furdyna, and L. R. Ram-Mohan, *Phys. Rev. Lett.* **68**, 3220 (1992).
- ⁴¹ S. D. Gunapala, B. F. Levine, and Naresh Chand, *J. Appl. Phys.* **70**, 305 (1991).